Journal of Computational Mathematics
Vol.30, No.3, 2012, 249–261.

http://www.global-sci.org/jcm
doi:10.4208/jcm.1111-m3714

AN OPTICAL FLOW APPROACH TO ANALYZING SPECIES DENSITY DYNAMICS AND TRANSPORT*

Aaron Luttman Erik Bollt
Department of Mathematics, Clarkson University, Potsdam, NY, USA
Email: aluttman21@gmail.com ebollt@clarkson.edu
Jason Holloway
Department of Electrical Engineering, Rice University, Houston, TX, USA
Email: jason.r.holloway@gmail.com

Abstract

Classical optical flow techniques were developed for computing virtual motion fields between two images of the same scene, assuming conservation of intensity and a smoothness of the flow field. If these assumptions are dropped, such techniques can be adapted to compute apparent flows between time snapshots of data that do not come from images, even if these flows are turbulent and divergent, as in the case of flows representing complex spatiotemporal dynamics. While imaging methods have been used to analyze dynamics in experimental applications, they are only beginning to be applied to dynamics computations in settings outside the laboratory, for example in the analysis of species population dynamics from satellite data. In this work we present a variational optical flow approach based on the continuity equation and total variation regularization for computing the flow fields between population densities generated from a two-species predator-prey model for phyto- and zooplankton interactions. Given the time-varying vector fields produced from the optical flow, computational methods from dynamical systems can be employed to study pseudo-barriers present in the species interaction. This method allows to measure the mixing of the species, as well as the transport of the populations throughout the domain.

Mathematics subject classification: 49N45, 49M99, 37M25, 65P99, 68T45.
Key words: Optical flow, Finite-time Lyapunov exponent, Mass transport, Data-driven dynamical systems.

1. Introduction

Variational optical flow methods are used to compute dense vector fields describing apparent motions between two adjacent images. The original optical flow algorithm, described by Horn and Schunck in [20], was based on the assumptions of local conservation of intensity and of the smoothness of the flow field. These assumptions are appropriate when the flow between the images is divergence-free, which is reasonable to assume for many rigid-body motions, particularly when the surfaces being imaged are not highly reflectant. The mathematical principle of optical flow, however, can serve as motivation and be adapted to compute flow fields between two different time snapshots of other kinds of data, even data that do not represent intensities *per se*.

One of the primary reasons to be interested in computing flow fields from non-image data is that in recent years new methods have been developed for analysis of dynamical systems from

* Received March 17, 2011 / Revised version received October 13, 2011 / Accepted November 3, 2011 / Published online May 7, 2012 /

the vector fields that describe the mass transport of the system. One such technique is the use of finite-time Lyapunov exponents (FTLE) [15] for discerning Lagrangian Coherent Structures (LCS) [16] in a dynamical system. The main idea behind the LCS computation is that it allows the detection and analysis of transport boundaries, describing a kind of time-varying region segmentation based on the dynamics of the system. That is, the coherent structures describe which regions of mass or density will flow together or mix in a system and which will flow away from each other. In most such analyses, the flow fields are derived directly from a system model using analytical techniques. In the absence of a model – or if the model used does not sufficiently capture the true dynamics – it is necessary to generate the governing flow field directly from measurements. This has been done using imaging techniques, for example, in particle image velocimetry (PIV) experiments [6, 24], but not for many applications outside of the laboratory. In particular, there is little work performing dynamics analysis directly from remotely sensed data in a model-free environment. The ability to perform such analysis would be particularly useful, since many dynamical systems are based on measured data with only approximate supporting *a priori* models or without any supporting models at all. In this work we adapt optical flow techniques to this end.

In order to demonstrate dynamics analysis using optical flow, we focus on a two-species predator-prey system of two partial differential equations in two unknown functions that model how the spatial densities of two species of plankton evolve in time. Given the density of one of the species at a particular time, optical flow techniques can be used to compute the virtual flow of the population density to the next discrete time step. In such a case, the flows of the densities are highly divergent and also have dynamic behavior not observed in classical optical flow applications, so it is necessary to adapt the current optical flow algorithms to allow for divergent flows and to capture dynamic structures such as vortices. The resulting flow fields are then used to compute the FTLE field for the flow as well as the density transport boundaries and pseudo-boundaries.

In this work, we demonstrate dynamics analysis from optical flow by generating synthetic data from a known model for plankton interactions. The model is used only for generating the data, and the optical flow and dynamics analysis are performed directly on the resulting densities, which are treated as measured data. This sample system is used to demonstrate the technique and to show that, if the system data were measured, for example by hyperspectral sensors, the dynamics could be computed directly from the measured intensities. Thus adapting methods such as optical flow from imaging science and computer vision is an ideal approach for analyzing the system dynamics, since such techniques can be generalized and applied directly to measured data. The primary advances of this work are the adaptation of optical flow to dynamical systems analysis for systems that are driven by data measured in an uncontrolled environment and the development of a computational approach suited to this application. Thus dynamics analysis which has previously been available only for systems with accurate models or in controlled laboratory environments can now be performed on model-free systems that are driven by data measured in uncontrolled environments.

In Section 2 the theoretical formulation of the variational optical flow approach is developed. The background, theory, and computational details of the LCS methodology are outlined in Section 3. Section 4 highlights the two-species predator-prey system for modeling phyto- and zooplankton population densities over time. The optical flow is computed directly from the generated data – and not from the model itself – serving as a test case for computing flow fields in the absence of models. The apparent flow fields are thus computed directly using optical

flow and the density dynamics are inferred from the resulting FTLE. The numerical techniques for computing the optimal optical flow field are presented in Section 5, and the results and conclusions are presented in Sections 6 and 7, respectively.

2. Total Variation-Regularized Optical Flow

Given time-varying intensity data, $I(x, y, t)$, on a spatial domain $\Omega \subset \mathbb{R}^2$, the original optical flow method proposed by Horn and Schunck in [20] was to compute the flow field $\mathbf{w} = \langle u, v \rangle$ that minimizes the energy

$$E_{\mathrm{HS}}(u, v) = \int_\Omega (I_t + I_x u + I_y v)^2 \, dA + \alpha \int_\Omega |\nabla u|^2 + |\nabla v|^2 \, dA, \tag{2.1}$$

where α is the regularization parameter and subscripts indicate partial derivatives. The first term is a data fidelity, which enforces the local conservation of intensity for divergence-free flow fields, and the second term is the regularization term, which ensures the smoothness of the flow. Many algorithms have been developed since to relax these assumptions, particularly by modifying the regularization term to capture the structure of non-smooth flows (see [1, 4, 23, 32–34] for a sample in what has become a vast literature).

More generally, a model for the underlying physical flow can be incorporated directly into the optical flow formulation; a framework for this is given in [18]. Specifically, we use an alternate data fidelity based on the continuity equation from fluid dynamics,

$$\frac{\partial I}{\partial t} + \operatorname{div}(I\mathbf{w}) = I_t + I_x u + I_y v + I u_x + I v_y = 0. \tag{2.2}$$

This was proposed by Corpetti et al. in [7], and, although it has been theoretically justified in only a few applications, the resulting optical flows have proven robust in many cases [8–10]. The resulting data fidelity is

$$E_{\mathrm{fid}}(u, v) = \int_\Omega (I_t + I_x u + I_y v + I u_x + I v_y)^2 \, dA. \tag{2.3}$$

Note that in the case of divergence-free flows, i.e. $\operatorname{div}(\mathbf{w}) = 0$, this reduces to the data fidelity of the Horn-Schunck algorithm, though the gradient of this functional does not reduce to the gradient of the conservation of intensity functional resulting in different optimization algorithms even when $\operatorname{div}(\mathbf{w}) = 0$. Just as in the case of local conservation of intensity, minimizing the continuity equation-based energy is not well-posed, and the functional must be enhanced with an appropriate regularization term.

Several different approaches have been developed for computing the optical flow of turbulent flow fields, such as the Navier-Stokes approach of Doshi et al. in [11] and the self-similar regularization approach of Heas, et al. in [19]. Past work for computing fluid optical flows can be found, for example in [2, 3, 21, 25], and in each case, the ability to capture the structures of vortices rests on extracting discontinuity information from the flow field. It is well-known that the regularizing of an energy functional with the total variation of the input function results in solutions that are approximately piecewise constant and that the jump discontinuities in the signal are enhanced (see [26, 27] for the original formulation and e.g. [5] for a recent and comprehensive overview of the use of total variation regularization in imaging). Thus we regularize using the total variation of the components of the flow field, and the optical flow

energy is given by

$$E(u,v) = \int_\Omega \left(I_t + I_x u + I_y v + I u_x + I v_y\right)^2 \, dA + \alpha \int_\Omega |\nabla u| + |\nabla v| \, dA. \tag{2.4}$$

We minimize this energy by computing a solution to the associated approximate Euler-Lagrange equations for u and v,

$$I\left(I_{tx} + I_{xx}u + 2I_x u_x + I_{yx}v + I_y v_x + I u_{xx} + I_x v_y + I v_{yx}\right) = -\frac{\alpha}{2}\nabla \cdot \frac{\nabla u}{\sqrt{|\nabla u|^2 + \epsilon}}, \tag{2.5}$$

$$I\left(I_{ty} + I_{xy}u + I_x u_y + I_{yy}v + 2I_y v_y + I_y u_x + I u_{xy} + I v_{yy}\right) = -\frac{\alpha}{2}\nabla \cdot \frac{\nabla v}{\sqrt{|\nabla v|^2 + \epsilon}}, \tag{2.6}$$

respectively. On the right-hand side, ϵ is a numerical regularization parameter resulting in a differentiable approximation to the total variation, and α is the theoretical regularization parameter, which serves as a weighting between the data fidelity and regularization energies. Direct minimization of (2.4) is also possible, using, for example, a hybrid lagged diffusivity fixed point iteration [31].

3. Lagrangian Coherent Structures

In this section we present the background theory and computational details for computing finite-time Lyapunov exponents and Lagrangian Coherent Structures for analyzing transport and mixing in a dynamical system.

The study of LCS was introduced by Haller and Haller-Yuan [16] as a mathematical formalism based on the theory of Finite Time Lyapunov Exponents (FTLE) [14–16]. The LCS are descriptive of finite-time attracting and repelling material surfaces and serve as finite-time analogues of hyperbolic invariant manifolds, which have been classically used to study transport in autonomous dynamical systems. The key point is that, given a vector field describing a nonautonomous dynamical system, the FTLE is a scalar field whose ridges represent pseudo-barriers across which transport is greatly hindered – a statement made formal by Shadden, Lekien, and Marsden in [29] – which can be used to segment the phase space into regions of related dynamical activity. This means that two particles starting in the same region of the exponent field will tend to flow together in time as the dynamical system evolves, whereas two particles straddling a ridge in the field – which corresponds to an LCS instability – will tend to diverge exponentially in time.

For a steady flow, the coherent structures extracted from the FTLE field approximate stable and unstable invariant manifolds of a hyperbolic fixed point, separating regions exhibiting qualitatively different activities. The flux of particles across an LCS approaches zero as the integration time for computation of the exponent field becomes larger [28,29]. These analytical tools allow us to quantify mixing in order to understand the dynamic mechanisms behind it.

Procedurally, the FTLE field is computed at each point in the computational domain directly from a vector field describing the flow at the point, and the ridges are computed using standard ridge regression techniques [14,16]. A scalar field of values is computed for each initial condition according to a deformation tensor corresponding to a specific time interval $0 \le t \le T$. In the setting of a two-dimensional velocity field on an invariant set $M \subset \mathbb{R}^2$, $\mathbf{w} = \langle u(x,y,t), v(x,y,t)\rangle$ is assumed to be an element of $C^2(\Omega)$, and the flow is given by

$$\frac{dx}{dt} = u(x,y,t) \quad \text{and} \quad \frac{dy}{dt} = v(x,y,t).$$

The corresponding flow, mapping over an epoch T, may be written $\phi_T \colon \mathbf{x}(t) \mapsto \mathbf{x}(t+T)$, and the strain tensor of the velocity field along the trajectory $\mathbf{x}(t)$ is given by the symmetric, time-dependent, 2×2 matrix

$$J_T = \frac{d\phi_T \mathbf{x}(t)^*}{dx} \frac{d\phi_T \mathbf{x}(t)}{dx}, \tag{3.1}$$

where $*$ denotes the operator adjoint. It is assumed that on some finite time interval the minimum and maximum eigenvalues, $\lambda_{\min}$ and $\lambda_{\max}$, of J_T satisfy the condition $\ln \lambda_{\min}(T) < 0 < \ln \lambda_{\max}$, which implies that there is compression in one direction and expansion in the transverse direction along the trajectory. This type of trajectory of a time-dependent velocity field is referred to as a hyperbolic trajectory [35]. The notation $\frac{d\phi_T \mathbf{x}(t)}{dx}$ describes the Jacobian derivative matrix of the time-T flow mapping from which

$$\left\| \frac{d\phi_T \mathbf{x}(t)}{dx} \right\|^2 = \lambda_{\max}(T) \tag{3.2}$$

defines the spectral norm of the Jacobian. The FTLE, which represents the maximum stretching at the point $\mathbf{x}(t)$ along the trajectory with duration time T, is given by

$$\sigma_T(\mathbf{x}(t)) = \frac{1}{|T|} \ln \sqrt{\lambda_{\max}(T)}. \tag{3.3}$$

Repelling and attracting LCS are defined according to [14,29] as the maximum ridges of FTLE computed in forward time ($T > 0$) and backward time ($T < 0$), respectively. Further, the flux integral of Shadden, Lekien, and Marsden [29] describes the transport across these pseudo-barriers and further the convergence to true barriers as $T \to \infty$.

4. Predator-Prey Model

A standard model describing the spatial population densities of interacting phyto- and zooplankton was proposed by Medvinski et al. in [22]. Given a fixed spatial domain Ω, the functions $P(x, y, t)$ and $Z(x, y, t)$ determine the population densities of the phyto- and zooplankton, respectively, at point (x, y) and time t, and, given appropriate initial conditions, the time evolution of the densities is given by the system

$$P_t = \triangle P + P(1 - P) + \frac{PZ}{P + h}, \qquad Z_t = \triangle Z + \frac{kPZ}{P + h} - mZ, \tag{4.1}$$

where m, k, and h are model parameters. This model illustrates a complex spatio-temporal dynamical system derived from the ecology of the interacting plankton, and the flow and transport properties of the density fields P and Z can be computed and analyzed using finite-time Lyapunov exponents, given vector fields describing the flows. Since the resulting functions represent densities, they can be measured as intensities by hyperspectral sensors. For example, phytoplankton densities can be inferred directly from chlorophyll measurements in the infrared spectrum. Thus the optical flow techniques described above can be used to compute the apparent density flows over time. The important point here is that the methods described in Section 2 are appropriate for computing the apparent flow directly from densities themselves. Thus the model is used only for generating the synthetic data, and our computations and analysis are performed directly on the data itself, without any analytic contribution by the model. Given the optical flow fields, the FLTE-LCS analysis described in Section 3 can be used to discuss

the mixing of the populations over time. Intuitively, if the phytoplankton population increases, one would expect the zooplankton population to increase as well, and visa versa, but the spatiotemporal interactions are more complicated. The coherent structures computed from the FTLE field are designed specifically to describe this interaction.

The model (4.1) is used as a benchmark data set. Given an initial population density state (i.e. initial condition to (4.1)), the system is integrated forward in time, yielding the time-evolution of the species population densities. These densities are taken as "measured data," and from this data the flow properties of the populations are inferred and the interactions of the populations are computed.

5. Numerical Implementation for Optical Flow

Given the measured data, the optical flow must be computed from the densities. The nonlinearity of Equations (2.5) and (2.6) due to the total variation terms in the energy (2.4) suggests that directly solving the Euler-Lagrange equations is impractical. Thus a gradient descent approach is used, computing the steady-state solution to the equations

$$\frac{\partial u}{\partial \tau} = I\left(I_{tx} + I_{xx}u + 2I_x u_x + I_{yx}v + I_y v_x + Iu_{xx} + I_x v_y + Iv_{yx}\right) + \frac{\alpha}{2}\nabla \cdot \frac{\nabla u}{\sqrt{|\nabla u|^2 + \epsilon}}, \quad (5.1)$$

$$\frac{\partial v}{\partial \tau} = I\left(I_{ty} + I_{xy}u + I_x u_y + I_{yy}v + 2I_y v_y + I_y u_x + Iu_{xy} + Iv_{yy}\right) + \frac{\alpha}{2}\nabla \cdot \frac{\nabla v}{\sqrt{|\nabla v|^2 + \epsilon}}, \quad (5.2)$$

where τ is an artificial time parameter of the descent (and t is the true time in the system evolution). We solve the equations using an explicit time-discretization and finite-difference approximations to the derivatives, assuming a zero normal derivative on the boundary. A general framework for this kind of formulation can be found in Weickert, et al. [32]. Given that the spatial grid for image data is fixed, it is necessary to use a sufficiently small time step in τ to maintain numerical stability, resulting in relatively slow convergence. A line search can be used at each iteration to adaptively select the time step, speeding up the convergence rate, but that is not done for the numerical experiments shown below.

Given the fact that image data has a fixed resolution, the spatial grid cannot be refined to improve the approximation given by the selected finite difference scheme. For this reason, we choose the approximations

$$\begin{aligned} u_x &\approx \frac{1}{12}\left(-u_{i,j+2} + 8u_{i,j+1} - 8u_{i,j-1} + u_{i,j-2}\right), \\ u_{xx} &\approx \frac{1}{12}\left(u_{i,j+2} - 16u_{i,j+1} + 30u_{i,j} - 16u_{i,j-1} + u_{i,j-2}\right), \\ u_{xy} &\approx \frac{1}{4}\left(u_{i-1,j-1} - u_{i-1,j+1} - u_{i+1,j-1} + u_{i+1,j+1}\right), \end{aligned} \quad (5.3)$$

with y derivatives computed similarly. The approximation to the mixed partial derivative is a second-order approximation, but the other two approximations are fourth-order. Note that we use standard matrix notation, i.e. x derivatives correspond to changes between columns and y derivatives to changes between rows. The spatial step sizes, Δx and Δy, are both taken to be 1, since the data exists on a regular rectangular grid, which can interpreted as if it were an image grid. In the examples shown below, the grid is 151×451, but, as will be described below, the computation is only sensitive to mesh size in the sense that too coarse a grid – with a paucity of data – results in poor flow field reconstructions.

There are several techniques that can be employed to compute the optimal regularization parameter α, which balances the minimization between fidelity to the measured data and the imposed regularity assumption. The *discrepancy principle* is the most mathematically rigorous but requires an *a priori* estimate on the input errors, which one typically does not have in applications. (See [12] for a general explanation of the discrepancy principle for inverse problems related to imaging.) Other possible methods are the *L-curve* method (see e.g. [17, 30]) or *Generalized Cross Validation* (see [13]), both of which are common in practice but lack universal mathematical justification. Optical flow computations are generally not sensitive to the choice of α, so in all experiments below we take $\alpha = 10^{-6}$. We also choose $\epsilon = 10^{-6}$ for numerical regularization.

6. Results

Given the system (4.1) and an initial density state, the population densities are integrated forward in time, and the initial transient dynamics are allowed to expire. The left-hand column of Fig. 6.1 shows two time snapshots of the phytoplankton density; brighter regions correspond to higher density. The image at the bottom of the left column is the computed optical flow between the two images (where flow directions have been plotted only for sufficiently large magnitudes).

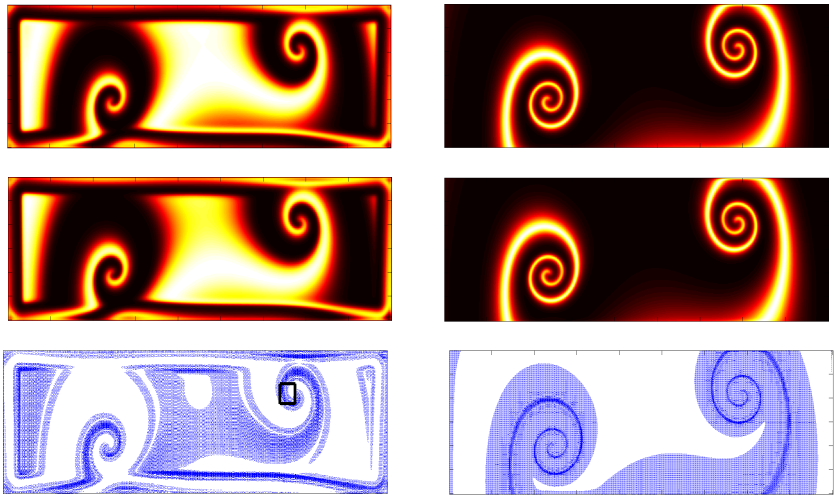

Fig. 6.1. Left–Phytoplankton Density at Two Adjacent Times and Computed Density Flow. A closeup of the boxed region can be seen in Fig. 6.2. Right–Zooplankton Density at Same Times and Computed Density Flow. The grid is 151×451 for all images in this section, unless otherwise specified.

Fig. 6.2 shows a closeup of the region boxed in Fig. 6.1. The computed vector field shows that the density is evolving outward, resulting in an apparent spiral of the phytoplankton population density.

The brightest regions of the two density images correspond to regions of highest population density, and notice that the flows of highest intensity correspond directly to the regions of highest density. Since the mass flow is proportional to the mass times the velocity, this implies that the highest mass transport occurs where there is the highest mass. The right-hand

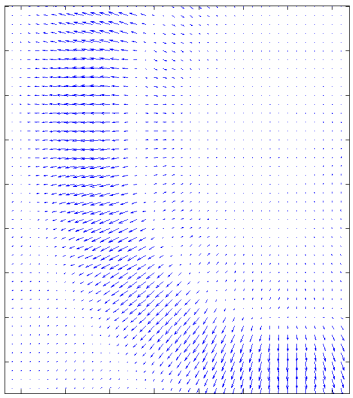

Fig. 6.2. Zoomed-in region of phytoplankton density flow, as highlighted in Fig. 6.1. Notice that the flow direction is radially outward along the spiral, which reflects the transport of the plankton population.

column of Fig. 6.1 shows the same time snapshots for the zooplankton density, as well as the corresponding flow. Again note that the highest densities correspond to the regions where the flow has largest magnitude.

It is important to note that the Continuity-TV algorithm (2.4) performs well for this application, in that the highest flows computed correspond precisely to the regions of highest density, which do in fact represent the largest mass transport in the system. Classical optical flow techniques, though essentially able to capture the dynamic structures in such a system, compute the highest flows in regions where the density gradient is highest, thus failing to capture the fact that large regions of high density may correspond to high flow.

In Fig. 6.4, the zooplankton flow corresponding to the densities on the right in Fig. 6.1 has been computed using the Horn-Schunck method (left). The Horn-Schunck technique captures only the outlines of the dynamic structures, i.e. the wave front and back, incorrectly producing

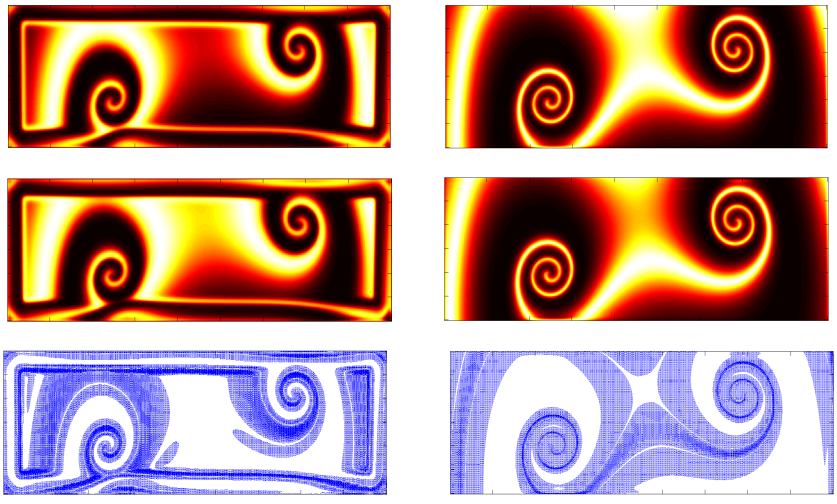

Fig. 6.3. Left–Phytoplankton Density at Two Adjacent Times Later in the System Evolution and Computed Density Flow. Right–Zooplankton Density at Same Times and Computed Density Flow

the light "trenches" of little to no flow in between. The results on the right in Fig. 6.4 were computed with a data fidelity that enforces conservation of intensity with a non-quadratic penalization and a flow driven anisotropic regularization (fidelity M_3 and regularizer S_5 in [32]). This method slightly outperforms the Horn-Schunck method and captures the main dynamic structures, but it also fails to compute the flow between wave fronts and wave backs, producing the incorrect trenches similar to those produced by Horn-Schunck.

In Fig. 6.3, two more time snapshots – later in the system evolution – are shown for the phytoplankton density and flow (left) and the zooplankton density and flow (right). Notice once again that the regions of highest density are correctly captured as being those of largest flow.

Fig. 6.5 reveals the FTLE fields for the phytoplankton (left) and zooplankton (right). On the right, the sources (dark) and sink (bright) reveal simple dynamics corresponding to two-dimensional unstable and stable manifolds. In this case there are no substantive pseudo-boundaries to the transport of the population in time. This makes sense, as the zooplankton are the predators, and there is no external force hindering their movement through the spatial domain. The phytoplankton FTLE, however, reveals a Lagrangian Coherent Structure as the ridge line that sweeps across on the left in Fig. 6.5. This corresponds to a time-dependent structure that essentially "pumps" the species through the domain as the spiral solutions spin. Such dynamics are not clear directly from the data, and performing the flow-based analysis is essential to computing such behavior in a dynamical system.

6.1. Sensitivity of Results to Grid Size

In Section 5, it was noted that the results are not particularly sensitive to the mesh size, except that too coarse a grid provides insufficient data for an accurate flow field reconstruction.

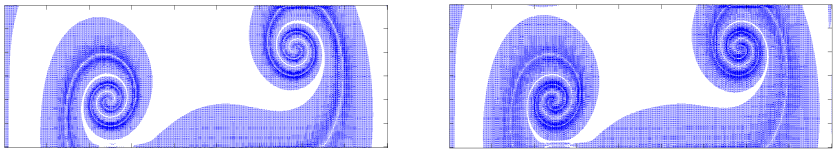

Fig. 6.4. Density Flow Between First Time Snapshots of Zooplankton, Computed Using (left) Horn-Schunck and (right) a Nonquadratic-Penalized Conservation of Intensity with Anisotropic Regularization (Weickert et al, [32], fidelity M_3 and regularization S_5). Note the gap in the center of the primary flow in each of these, indicating that there is little flow, which is clearly not the case. The central flow is correctly captured as the most intense part of the flow using the algorithm proposed here, as seen in the lower right of Fig. 6.1.

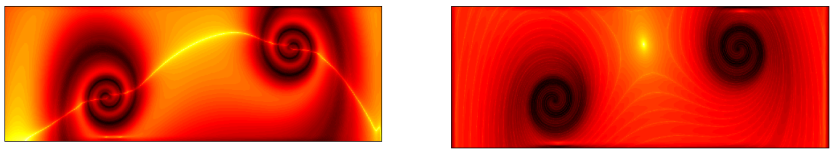

Fig. 6.5. LCS Results for Phytoplankton (left) and Zooplankton (right). A Lagrangian Coherent Structure in the phytoplankton dynamics is shown as the ridge line across the middle of the image. For the zooplankton, stable and unstable manifolds are shown, corresponding to the sources and sinks.

In Fig. 6.6, we show the results of the flow computation for the zooplankton density, using four different spatial scales (image (a) being computed from the highest resolution $\{141 \times 201$ grid cells$\}$, with images (b), (c), and (d) in dyadically decreasing resolutions). The four images are zoomed in a small region of the population, in order to better see how the flow reconstructions relate. It is readily seen that the three highest resolutions show essentially the same flow structures, whereas the smallest resolution is too coarse to contain the flow information.

In order to quantify this comparison, we use the highest resolution as a baseline computation, and we compare the angles of the flow vectors in each of the lower resolution computations to the angles computed from the correspondingly subsampled highest resolution. Thus, for each flow vector at a lower resolution, we compute the angle between that vector and its counterpart in the highest resolution. This deviation is the angular error associated with the change in grid size, and it essentially measures difference between subsampling the data and computing the flow versus computing the flow and subsampling the data. The median errors for each of the three lower resolutions are shown in Table 6.1, and the point of interest is that the median angular error does not monotonically increase with decreasing resolution.

Table 6.1: Median angular error between flow vectors computed from low resolution data and flow vectors subsampled from highest resolution data. The error for Resolution (a) is 0°, because that is the highest resolution computation, which is used as the baseline comparison for the other resolutions. Thus Resolution (a) compared to Resolution (a) will naturally result in no error. Note that decreasing the resolution does not monotonically increase the median angular error.

	Resolution (a)	Resolution (b)	Resolution (c)	Resolution (d)
Median Angular Error	0°	1.0206°	1.9249°	1.0231°

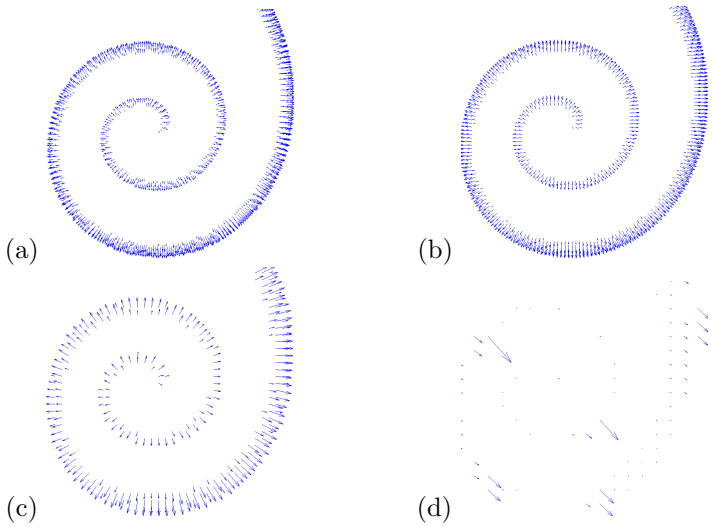

Fig. 6.6. Zooplankton flow computed from four different resolutions. Image (a) is the highest, with (b), (c), and (d) sequentially decreasing in resolution vertically and horizontally by a factor of 2. In each case, only the flow vectors whose magnitude is larger than twice the mean magnitude (over the entire spatial domain) are shown. As can be seen, the first three images show that the flow dynamics captured are essentially the same. It is not clear that the lowest resolution – shown in image (d) – also captures the flow, but in fact it does (see Fig. 6.7).

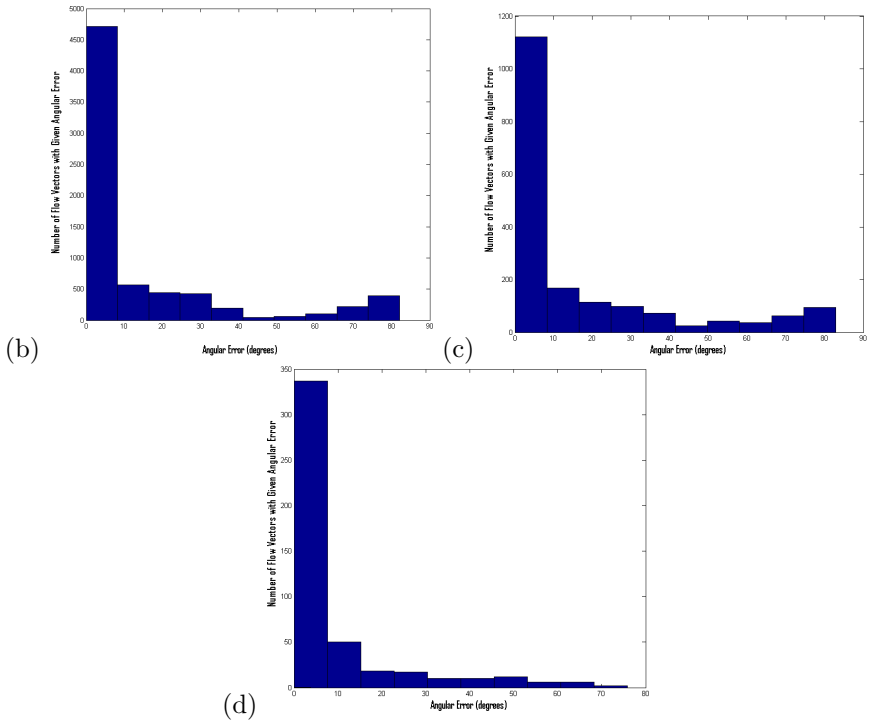

Fig. 6.7. Histogram of angular errors for grid resolutions (b), (c), and (d), using the highest resolution as the baseline. For each flow vector at the lower resolutions, the angle between that vector and the corresponding flow vector in the highest resolution is computed. This is the angular error. In each case, a very large majority of flow vectors at the lower resolutions deviate only small amounts from their counterparts at the highest resolution. Note that the distribution does not change significantly as the resolution decreases. There is no histogram for Resolution (a), since Resolution (a) is the baseline for comparison.

In Fig. 6.7, we show the angular error histograms for each of the three lower resolutions, compared to the highest resolution. The distribution of angular errors does not skew with decreasing resolution, which shows that even the lowest resolution for this case (which is 18×26 grid cells) is capturing the same dynamics as the highest resolution. This was not evident in Fig. 6.6.

Essentially, the moral of this story is that the flow computation is not sensitive to the grid resolution, up to the scale of the flow dynamics.

7. Conclusions

Optical flow techniques can be adapted to allow for divergent flow and to capture dynamic structures such as vortices, and such hybrid techniques are applicable for computing flow fields between time snapshots of many different kinds of data, including intensity data (e.g. images) but also density data, such as that produced by dynamical systems with complex spatiotemporal dynamics. The dynamics of these systems can then be quantified and analyzed using computational techniques that are normally applied to systems described analytically. In this work we have presented a variational optical flow technique well-suited to capturing the dy-

namics in a system driven by the data itself, as well as the corresponding results for a specific predator-prey system.

Acknowledgments. The authors would like to thank Sean Kramer for providing the predator-prey simulation data, as well as the anonymous referees for their helpful comments and suggestions for improving the manuscript.

References

[1] T. Amiaz and N. Kiryati, Piecewise-smooth dense optical flow via level sets, *Int. J. Computer Vision*, **68** (2006), 111–124.

[2] D. Auroux, Extraction of velocity fields for geophysical fluids from a sequence of images, in *Acoustics, Speech, and Signal Processing, IEEE Proceedings on (ICASSP)*, 2009, 961–964.

[3] D. Auroux and J. Fehrenbach, Identification of velocity fields for geophysical fluids from a sequence of images, *Experiments in Fluids*, **50** (2011), 313–328.

[4] T. Brox, A. Bruhn, N. Papenberg, and J. Weickert, High accuracy optical flow estimation based on a theory for warping, in T. Pajdla and J. Matas, editors, *Proc. 8th Eur. Conf. on Computer Vision*, **4** (2004), 25–36.

[5] T. Chan and J. Shen, Image Processing and Analysis: Variational, PDE, Wavelet, and Stochastic Methods, SIAM, 2005.

[6] T. Corpetti, D. Heitz, G. Arroyo, E. Mémin, and A. Santa-Cruz, Estimation of motion using a PIV correlation-based method and an "optical-flow" one for two experimental flows: quantitative and qualitative comparison, in *12th International Symposium on Applications of Laser Techniques to Fluid Mechanics*, 2004, 1–14.

[7] T. Corpetti, É. Mémin, and P. Pérez, Adaptation of standard optic flow methods to fluid motion, in *9th Int. Symp. Flow Visualisation*, paper 62, 2000, 1–10.

[8] T. Corpetti, É. Mémin, and P. Pérez, Estimating fluid optical flow, in *ICPR*, 2000, 7045–7048.

[9] T. Corpetti, É. Mémin, and P. Pérez, Dense estimation of fluid flows, *IEEE Trans. Pattern Anal. Machine Intelligence*, **24** (2002), 365–380.

[10] T. Corpetti, É. Mémin, and P. Pérez, Dense motion analysis in fluid imagery, in A. Heyden, editor, *Proc. 7th Eur. Conf. Computer Vision*, 2002, 676–691.

[11] A. Doshi and A. G. Bors, Navier-Stokes formulation for modelling turbulent optical flow, in *BMVC07*, 2007, 1–10.

[12] H. W. Engl, Discrepancy principles for Tikhonov regularization of ill-posed problems leading to optimal convergence rates, *Journal of optimization theory and applications*, **52** (1987), 209–215.

[13] G. Golub, M. Heath, and G. Wahba, Generalized cross-validation as a method for choosing a good ridge parameter, *Technometrics*, **21** (1979), 215–223.

[14] G. Haller, Lagrangian coherent structures from approximate velocity data, *Physics of Fluids*, **14** (2002), 1851–1861.

[15] G. Haller and A. C. Poje, Finite time transport in aperiodic flows, *Physica D: Nonlinear Phenomena*, **119** (1998), 352–380.

[16] G. Haller and G. Yuan, Lagrangian coherent structures and mixing in two-dimensional turbulence, *Physica D: Nonlinear Phenomena*, **147** (2000), 352–370.

[17] P.C. Hansen, The L-curve and its use in the numerical treatment of inverse problems, in P. Johnston, editor, *Computational Inverse Problems in Electrocardiology, Advances in Computational Bioengineering*, 2000, 119–142.

[18] H.W. Haussecker and D.J. Fleet, Computing optical flow with physical models of brightness variation, *IEEE Transactions on Pattern Analysis and Machine Intelligence*, **23** (2001), 661–673.

[19] P. Héas, É. Mémin, and D. Heitz, Self-similar regularization of optic-flow for turbulent motion estimation, in *The 1st International Workshop on Machine Learning for Vision-based Motion*

Analysis, Marseille, France, 2008, 1–12.

[20] B.K.P. Horn and B.G. Schunck, Determining Optical Flow, *Artificial Intelligence*, **17** (1981), 185–203.

[21] F. Li, L. Xu, P. Guyenne, and J. Yu, Recovering fluid-type motions using Navier-Stokes potential flow, in *Computer Vision and Pattern Recognition, IEEE Computer Society Conference on*, 2010, 2448–2455.

[22] A.B. Medvinski, S.V. Petrovskii, I.A. Tikhonova, H. Malchow, and B. Li, Spatiotemporal complexity of plankton and fish dynamics, *SIAM Review*, **44** (2002), 311–370.

[23] M. Proesmans, L. Van Gool, E. Pauwels, and A. Oosterlinck, Determination of optical flow and its discontinuities using nonlinear diffusion, in *Proc. Third Eur. Conf. Computer Vision*, 1994, 295–304.

[24] G.M. Quénot, J. Pakleza, and T. A. Kowalewski, Particle image velocimetry with optical flow, *Experiments in Fluids*, **25** (1998), 177–189.

[25] T. Regert, B. Tremblais, and L. David, Parallelized 3D optical flow method for fluid mechanics applications, in *Fifth International Symposium on 3D Data Processing, Visualization and Transmission*, 2010, 1–8.

[26] L. Rudin and S. Osher, Total Variation Based Image Restoration with Free Local Constraints, in *Proc. 1st IEEE ICIP*, **1** (1994), 31–35.

[27] L. Rudin, S. Osher, and E. Fatemi, Nonlinear total-variation based noise removal algorithms, *Physica D: Nonlinear Phenomena*, **60** (1992), 259–268.

[28] S.C. Shadden, J.O. Dabiri, and J.E. Marsden, Lagrangian analysis of fluid transport in empirical vortex ring flows, *Physics of Fluids*, **18** (2006), 1–11.

[29] S.C. Shadden, F. Lekien, and J.E. Marsden, Definition and properties of Lagrangian coherent structures from finite-time Lyapunov exponents in two-dimensional aperiodic flows, *Physica D: Nonlinear Phenomena*, **212** (2005), 271–304.

[30] C.R. Vogel, Non-convergence of the L-curve regularization parameter selection method, *Inverse Problems*, **12** (1996), 535–547.

[31] C.R. Vogel, Computational Methods for Inverse Problems, Frontiers in Applied Mathematics, SIAM, 2002.

[32] J. Weickert, A. Bruhn, N. Papenberg, and T. Brox, Variational optic flow computation: From continuous models to algorithms, in L. Alvarez, editor, *International Workshop on Computer Vision and Image Analysis, IWCVIA03, Las Palmas de Gran Canaria*, 2003, 1–6.

[33] J. Weickert and C. Schnörr, Variational optical flow computation with a spatio-temporal smoothness constraint, *Journal of Mathematical Imaging and Vision*, **14** (2001), 245–255.

[34] J. Weickert and C. Schnörr, A theoretical framework for convex regularizers in PDE-based computation of image motion, *International Journal of Computer Vision*, **45** (2001), 245–264.

[35] S. Wiggins, Introduction to Applied Nonlinear Dynamical Systems and Chaos, Springer Verlag, 2003.